CrossMark

Possible Systematic Rotation in the Mature Stellar Population of a $z = 9.1$ Galaxy

Tsuyoshi Tokuoka[1], Akio K. Inoue[1,2], Takuya Hashimoto[3], Richard S. Ellis[4], Nicolas Laporte[5,6], Yuma Sugahara[2,7], Hiroshi Matsuo[7], Yoichi Tamura[8], Yoshinobu Fudamoto[2,7], Kana Moriwaki[9], Guido Roberts-Borsani[10], Ikkoh Shimizu[11], Satoshi Yamanaka[12], Naoki Yoshida[9,13,14,15], Erik Zackrisson[16], and Wei Zheng[17]

[1] Department of Pure and Applied Physics, Graduate School of Advanced Science and Engineering, Faculty of Science and Engineering, Waseda University, 3-4-1, Okubo, Shinjuku, Tokyo 169-8555, Japan; akinoue@aoni.waseda.jp
[2] Waseda Research Institute for Science and Engineering, Faculty of Science and Engineering, Waseda University, 3-4-1, Okubo, Shinjuku, Tokyo 169-8555, Japan
[3] Tomonaga Center for the History of the Universe (TCHoU), Faculty of Pure and Applied Sciences, University of Tsukuba, Tsukuba, Ibaraki 305-8571, Japan
[4] Department of Physics & Astronomy, University College London, Gower Street, London WC1E 6BT, UK
[5] Kavli Institute for Cosmology, University of Cambridge, Madingley Road, Cambridge CB3 0HA, UK
[6] Cavendish Laboratory, University of Cambridge, 19 JJ Thomson Avenue, Cambridge CB3 0HE, UK
[7] National Astronomical Observatory of Japan, 2-21-1, Osawa, Mitaka, Tokyo 181-8588, Japan
[8] Division of Particle and Astrophysical Science, Graduate School of Science, Nagoya University, Aichi 4648602, Japan
[9] Department of Physics, The University of Tokyo, 7-3-1 Hongo, Bunkyo, Tokyo 113-0033, Japan
[10] Department of Physics and Astronomy, University of California, Los Angeles, 430 Portola Plaza, Los Angeles, CA 90095, USA
[11] Department of Literature, Shikoku Gakuin University, 3-2-1 Bunkyocho, Zentsuji, Kagawa 765-8505, Japan
[12] General Education Department, National Institute of Technology, Toba College, 1-1, Ikegami-cho, Toba, Mie 517-8501, Japan
[13] Kavli Institute for the Physics and Mathematics of the Universe (WPI), UT Institutes for Advanced Study, The University of Tokyo, 5-1-5 Kashiwanoha, Kashiwa, Chiba 277-8583, Japan
[14] Research Center for the Early Universe, School of Science, The University of Tokyo, 7-3-1 Hongo, Bunkyo, Tokyo 113-0033, Japan
[15] Institute for Physics of Intelligence, School of Science, The University of Tokyo, 7-3-1 Hongo, Bunkyo, Tokyo 113-0033, Japan
[16] Observational Astrophysics, Department of Physics and Astronomy, Uppsala University, Box 516, SE-751 20 Uppsala, Sweden
[17] Department of Physics and Astronomy, Johns Hopkins University, Baltimore, MD 21218, USA

Abstract

We present new observations with the Atacama Large Millimeter/submillimeter Array for a gravitationally lensed galaxy at $z = 9.1$, MACS1149-JD1. [O III] 88 μm emission is detected at 10σ with a spatial resolution of ~ 0.3 kpc in the source plane, enabling the most distant morphokinematic study of a galaxy. The [O III] emission is distributed smoothly without any resolved clumps and shows a clear velocity gradient with $\Delta V_{obs}/2\sigma_{tot} = 0.84 \pm 0.23$, where ΔV_{obs} is the observed maximum velocity difference and σ_{tot} is the velocity dispersion measured in the spatially integrated line profile, suggesting a rotating system. Assuming a geometrically thin self-gravitating rotation disk model, we obtain $V_{rot}/\sigma_V = 0.67^{+0.73}_{-0.26}$, where V_{rot} and σ_V are the rotation velocity and velocity dispersion, respectively, still consistent with rotation. The resulting disk mass of $0.65^{+1.37}_{-0.40} \times 10^9 M_\odot$ is consistent with being associated with the stellar mass identified with a 300 Myr old stellar population independently indicated by a Balmer break in the spectral energy distribution. We conclude that the most of the dynamical mass is associated with the previously identified mature stellar population that formed at $z \sim 15$.

Unified Astronomy Thesaurus concepts: Galaxy formation (595); Galaxy dynamics (591); Galaxy evolution (594); High-redshift galaxies (734)

1. Introduction

The Atacama Large Millimeter/submillimeter Array (ALMA) has revolutionized high-redshift galaxy observations, allowing galaxies to be characterized well into the epoch of reionization. For example, dust continuum as well as the [O III] 88 μm and [C II] 158 μm emission lines of galaxies at $z > 7$ have been successfully observed (e.g., Watson et al. 2015; Inoue et al. 2016; Hashimoto et al. 2019). In particular, MACS1149-JD1 (Zheng et al. 2012; Bouwens et al. 2014; Huang et al. 2016; Zheng et al. 2017; Hoag et al. 2018) is a gravitationally lensed galaxy emitting the [O III] line at $z = 9.1$, one of the most distant objects spectroscopically confirmed (Hashimoto et al. 2018, hereafter H18). This galaxy also shows a Balmer break consistent with a stellar population of a few hundred Myr old,

suggesting its formation epoch is $z \sim 15$ (H18; Binggeli et al. 2019; Roberts-Borsani et al. 2020; Laporte et al. 2021).

Beyond finding high-redshift galaxies, studying their dynamics based on the kinematics of their interstellar medium provides further motivation for probing the early physics of galaxy formation. Such studies have been mostly conducted with three-dimensional (3D) near-infrared spectroscopy for galaxies at $z < 4$ (e.g., Förster Schreiber et al. 2009; Jones et al. 2010; Wisnioski et al. 2015). However, the high sensitivity and high spatial and frequency resolution of ALMA also make it possible to analyze morphokinematics of galaxies at $4 < z < 6$ (Rizzo et al. 2020, 2021; Lelli et al. 2021) and even at $z \sim 7$ (Smit et al. 2018). In this Letter, we present the most distant example of a morphokinematic analysis of the [O III] emission in MACS1149-JD1 at $z = 9.1$ and discuss when the rotational motion in galaxies first appears.

Throughout this Letter, we use a flat ΛCDM cosmology with a parameter set of $(h, \Omega_m, \Omega_\Lambda) = (0.704, 0.272, 0.728)$ (Komatsu et al. 2011).
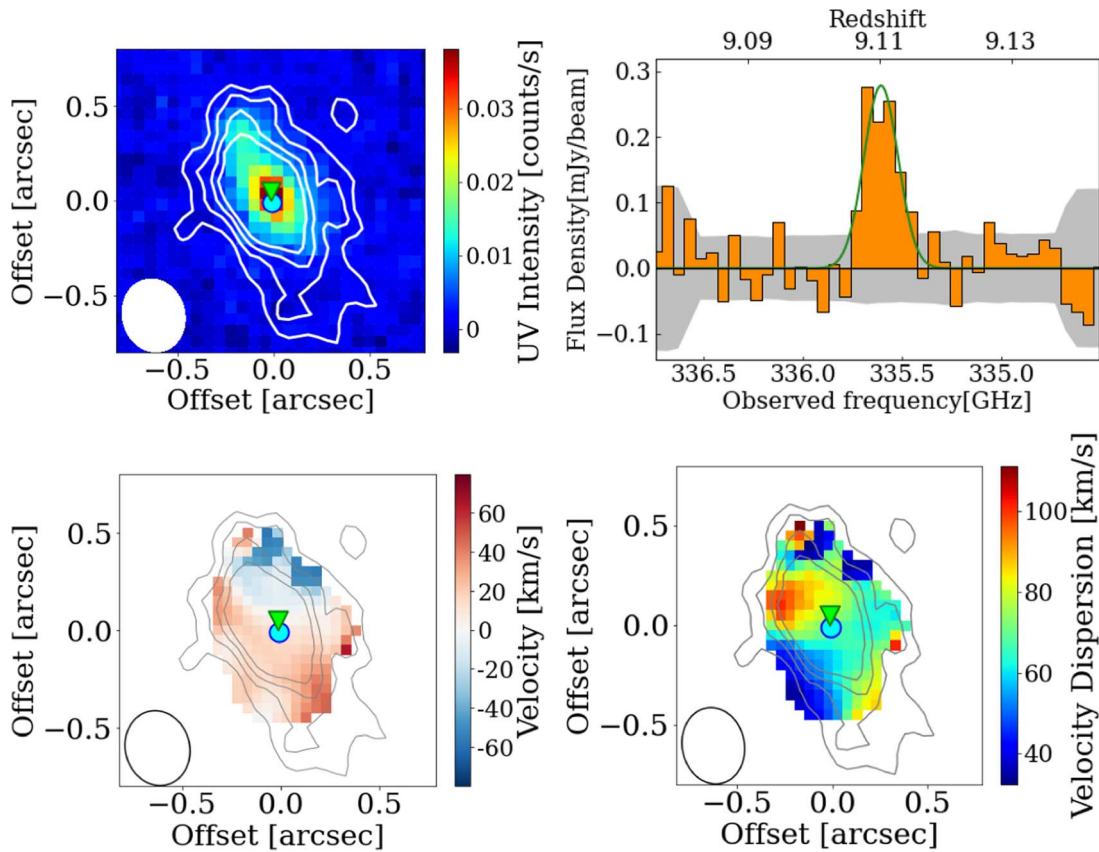
Figure 1. Top left: ALMA [O III] 88 μm emission moment-0 map contours on the HST/WFC3 F160W image of MACS1149-JD1 at $z = 9.1$. The contours show $+3\sigma$, 4σ, 5σ, and 6σ with $\sigma = 9.4$ mJy km s^{-1} beam^{-1}. The synthesized beam ellipse is shown in the bottom left corner. The circle and inverse-triangle indicate the centers of [O III] emission dynamical disk (Section 4) and ultraviolet (UV) emission, respectively. Top right: [O III] line spectrum integrated over the area where the line was detected at $>3\sigma$. The gray shaded region indicates the $\pm1\sigma$ noise level. The solid curve is the best-fit Gaussian profile. Bottom left: [O III] line velocity field overlaid on the line moment-0 contours. The velocity field is depicted only in the area where the Gaussian line profile fitting is favored with confidence $>5\sigma$ (see Section 3). Bottom right: [O III] line velocity dispersion map overlaid on the line moment-0 contours. The depicted area is the same as the velocity field.

2. Observational Data

New observations for [O III] 88 μm emission from MACS1149-JD1 were performed in Band 7 during ALMA Cycle 6 (2018.1.00616.S, PI: T. Hashimoto) to improve the spatial resolution of the emission line. The antenna configurations were C43-4, -5, and -6 (minimum baseline $= 15.1$ m and maximum baseline $= 783.5$–2516.9 m). We set a spectral window (SPW) centered at a 335.625 GHz emission line frequency (H18) with a bandwidth of 1.875 GHz and 240 channels, corresponding to a velocity resolution of 7.0 km s^{-1}. Three other SPWs were set at the central frequencies of 337.375, 347.417, and 349.176 GHz to obtain the continuum emission, with bandwidths of 2.000 GHz and 128 channels. The observations were executed in a series of 13 sets between 2018 October 18 and December 15. The precipitable water vapor during the observations spread over 0.3–1.0 mm, and the mean was 0.5 mm. The total on-source exposure time was 9.6 hr, compared to 2.0 hr in the previous observations (H18). Raw data were processed using Common Astronomy Software Applications (CASA; McMullin et al. 2007) version 5.4.0–68, Pipeline version 42030M.

3. Data Analysis

3.1. Overview of New Results

First, we created a dust continuum image from all data using CASA task tclean, which resulted in a null detection. A new

3σ upper limit on the dust continuum is 19 μJy beam^{-1}, a factor of 3 improvement over the previous limit (H18). Next, we created a data cube from the Cycle 6 SPWs supposed to contain the [O III] line using tclean with natural weighting and 50 km s^{-1} velocity binning. We successfully confirmed the [O III] line in this independent data set. The redshift is $z = 9.1111 \pm 0.006$, which is consistent with $z = 9.1096 \pm 0.006$ found by H18. Combining all SPWs of H18 and Cycle 6 data, which contain the [O III] line, we also created a data cube using tclean with natural weighting and 50 km s^{-1} velocity binning. We use this "dirty" imaging data cube throughout this Letter.[18]

We created a velocity-integrated intensity map, i.e., moment-0 map, of the [O III] line (Figure 1, top left) using CASA task immoments from the data cube within a velocity range of -150 to $+200$ km s^{-1} relative to the line redshift $z = 9.1096$ (H18). We also extracted the total line spectrum (Figure 1, top right) from the data cube integrated over the area where the line emission was detected at $>3\sigma$ in the moment-0 map. The velocity dispersion of the total line profile was measured at $\sigma_{\rm tot} = 72.7 \pm 8.1$ km s^{-1}, also consistent with 65.4 ± 16.6 km s^{-1} in H18.

---

[18] We use the "dirty" beam to convolve the dynamical model in Section 4, avoiding any biases induced by modeling of the "clean" beam for the "clean" data cube, which is not straightforward for the combined data sets of different array configurations.

In the moment-0 map, the peak signal-to-noise ratio increased from 7.4σ (H18) to 10σ, and the beam FWHM improved from $0\rlap{.}''62 \times 0\rlap{.}''52$ (H18) to $0\rlap{.}''39 \times 0\rlap{.}''33$. The deconvolved FWHM of the emission was measured at $0\rlap{.}''81 \times 0\rlap{.}''47$, consistent with H18. Therefore, the ionized gas is distributed smoothly without clumps, even in the improved resolution.

3.2. Velocity Field

To examine the velocity structure of MACS1149-JD1, we adopted a method of Smit et al. (2018): a Gaussian line profile fit for the spectrum at each spatial pixel in the dirty data cube. We selected spatial pixels, where a $>5\sigma$ significance of the Gaussian fit was obtained. Namely, $\Delta\chi^2 = \chi^2_{\mathrm{no\ line}} - \chi^2_{\mathrm{Gauss}} \geqslant 25$, where $\chi^2_{\mathrm{no\ line}} = \sum_i \frac{|I_{\mathrm{obs}}(V_i) - I_{\mathrm{cont}}|^2}{\delta^2_{I_{\mathrm{obs}}(V_i)}}$ and $\chi^2_{\mathrm{Gauss}} = \sum_i \frac{|I_{\mathrm{obs}}(V_i) - \{I_{\mathrm{cont}} + I_{\mathrm{Gauss}}(V_i)\}|^2}{\delta^2_{I_{\mathrm{obs}}(V_i)}}$. $I_{\mathrm{obs}}(V_i)$ and $I_{\mathrm{Gauss}}(V_i)$ are, respectively, the observed intensity and Gaussian line profile at velocity V_i. I_{cont} is the continuum level, and we set it to zero because of its null detection. $\delta_{I_{\mathrm{obs}}(V_i)}$ is the observed uncertainty of the intensity at velocity V_i, which was measured as the rms in the velocity channel of the dirty cube. The resultant maps of the line velocity and the velocity dispersion are shown in the bottom left and right panels in Figure 1, respectively. There is a clear velocity gradient along the north–south direction. The maximum velocity difference was measured at $\Delta V_{\mathrm{obs}} = 122 \pm 30$ km s^{-1}. The uncertainty was calculated from those of the reddest and bluest velocities. The velocity dispersion ranges from a few tens to a hundred km s^{-1}, and its average is ~ 70 km s^{-1}.

We have obtained a kinematic ratio of $\Delta V_{\mathrm{obs}}/2\sigma_{\mathrm{tot}} = 0.84 \pm 0.23$, which is a factor of 1.5 greater than those observed in two rotation-dominated galaxies at $z \sim 7$ reported by Smit et al. (2018), as shown in the top panel of Figure 2. The ratio is also $\sim 2\sigma$ above a criterion for determining whether a galaxy is rotation or dispersion dominated, $(\Delta V_{\mathrm{obs}}/2\sigma_{\mathrm{tot}})_{\mathrm{crit}} = 0.4$, empirically derived from a set of simulations and Hα line observations of galaxies (e.g., Förster Schreiber et al. 2009; Smit et al. 2018).

4. Dynamical Modeling

4.1. Procedure

Motivated by the large kinematic ratio indicative of a rotation-dominated system (Section 3), we performed dynamical modeling of MACS1149-JD1, assuming a geometrically thin rotating disk. The model constraint was obtained by fitting the 3D dirty data cube, rather than the two-dimensional (2D) velocity field, to avoid rotational velocity underestimation and velocity dispersion overestimation due to the beam smearing effect (Di Teodoro & Fraternali 2015). The fitting procedure comprises four steps: (1) construction of a model of the 3D emission line data cube in the source plane, (2) coordinate mapping from the source plane to the image plane using a gravitational lensing model, (3) convolution with the dirty beam profile in the image plane, and (4) optimization. Before explaining each step below, we summarize the nine fitting parameters in the modeling: M_{disk} (mass), r_{disk} (scale length), i_{disk} (inclination), PA_{disk} (position angle), x_0, y_0 (central position), A_0 ([O III] intensity at the disk center), σ_V (velocity dispersion), and ΔV_{sys} (velocity offset from the systemic redshift).
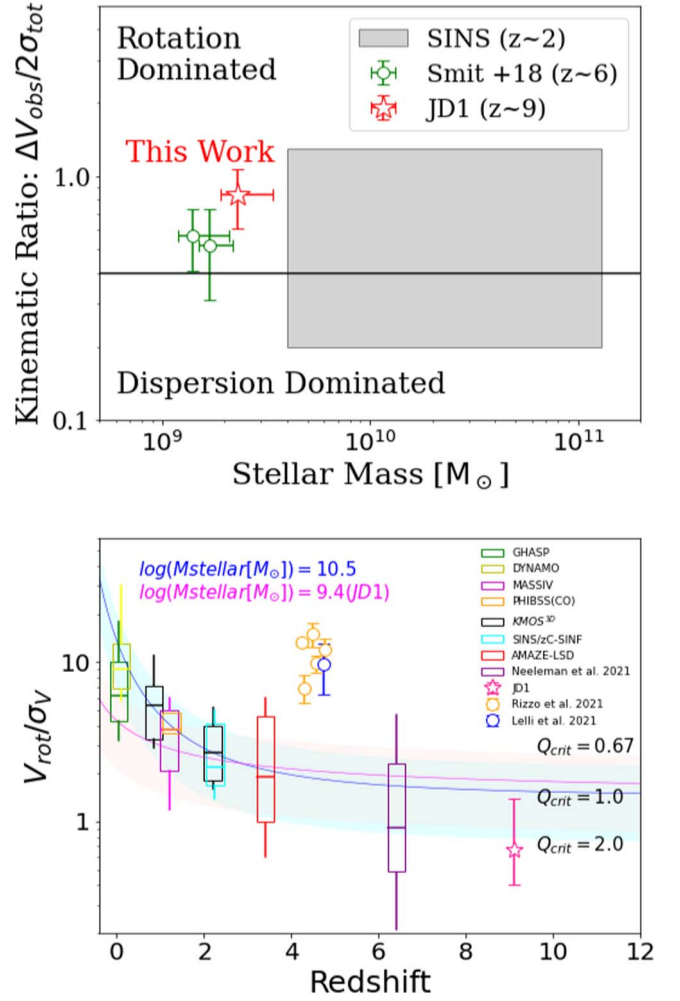
Figure 2. (Top) Observed kinematic ratio, $\Delta V_{\mathrm{obs}}/2\sigma_{\mathrm{tot}}$, as a function of the stellar mass. Our measurement of MACS1149-JD1 shown by the five-pointed star is compared with those of two $z \sim 6$ galaxies (Smit et al. 2018) shown by the circles and the distribution of measurements of $z \sim 2$ star-forming galaxies (Förster Schreiber et al. 2009) shown by the shaded area. The horizontal line at $\Delta V_{\mathrm{obs}}/\sigma_{\mathrm{tot}} = 0.4$ is an empirical boundary between the rotation-dominated and dispersion-dominated systems (Förster Schreiber et al. 2009). (Bottom) Kinematic ratio, $V_{\mathrm{rot}}/\sigma_V$, based on dynamical modeling (Section 4) as a function of redshift. The estimation for MACS1149-JD1 is shown by the five-pointed star. The box plots at $z < 4$ are taken from Wisnioski et al. (2015) and show the median (middle bar) as well as the central 50th percentile (box) and 90th percentile (vertical lines) of the sample distribution in each survey (see Wisnioski et al. 2015 for the references). The box plot at $z \sim 6$ is the result of quasar host galaxies (Neeleman et al. 2021). The circles at $z \sim 4.5$ are results of massive rotational galaxies (Lelli et al. 2021; Rizzo et al. 2021). The blue and magenta solid lines show semiempirical models based on Toomre's disk instability parameter, $Q_{\mathrm{crit}} = 1.0$ (quasistable thin gas disk; Wisnioski et al. 2015) with stellar masses of $10^{10.5}$ $M_\odot$ and $10^{9.4}$ $M_\odot$, respectively. The shaded areas around the lines indicate the range of $Q_{\mathrm{crit}} = 0.67$ (thick gas disk) and $Q_{\mathrm{crit}} = 2.0$ (star and gas composite disk) cases (Wisnioski et al. 2015).

The construction of the line data cube was made by adopting Freeman's formula for the velocity field along the radial coordinate (Freeman 1970). Namely, we assumed a geometrically thin, self-gravitating rotation disk with an exponential surface mass distribution along the radial distance, which is described by M_{disk}, r_{disk}, i_{disk}, and PA_{disk}. The maximum rotation velocity of the disk, V_{rot}, is calculated from M_{disk} and r_{disk} by $V_{\mathrm{rot}} = 0.88\sqrt{GM_{\mathrm{disk}}/2r_{\mathrm{disk}}}$ (Freeman 1970), where G is the gravitational constant. We allowed a spatial offset of the disk center (x_0, y_0) from a reference point in the source plane.

The [O III] line velocity field was given by this disk model, and the line profile was assumed to be a Gaussian function with a constant velocity dispersion, σ_V, throughout the system. We allowed a constant velocity offset, $\Delta V_{\rm sys}$, from the line redshift of $z = 9.1096$ (H18). The velocity-integrated [O III] line intensity distribution is assumed to follow the surface mass distribution of the dynamical disk with the last parameter describing the central line intensity, A_0.

Coordinate mapping was performed by adopting lensing models (convergence, κ, and shear, γ_1 and γ_2) of the MACS1149 cluster released by the Hubble Frontier Field (HFF) project (Lotz et al. 2017).[19] We confirmed that all six lensing models in the HFF gave qualitatively same results. In this Letter, we present the results with the model of Kawamata et al. (2015) based on `glafic` (Oguri 2010).

Convolution with the dirty beam in the image plane was performed to the constructed line data cube model. We adopted a synthesized dirty beam model at a velocity of 0 km s^{-1} in the observed dirty data cube.

Optimization was performed using a least-squares method based on the Levenberg–Marquardt algorithm in a package of `scipy.optimize.least_squares`.[20] The model fitting was done in the image plane by comparing the modeled dirty cube with the observed cube in the velocity range of -150 to $+200$ km s^{-1} with a 50 km s^{-1} binning. The spatial area used in the fitting was the region where the [O III] line was detected at $>3\sigma$ (i.e., the region enclosed by the outermost contour in the top left panel of Figure 1). The chi-square was defined by $\sum_{i,j,k} |I_{i,j}^{\rm obs}(V_k) - I_{i,j}^{\rm model}(V_k)|^2 / \delta_{I_{i,j}^{\rm obs}(V_k)}^2$, where $I_{i,j}^{\rm model}(V_k)$, $I_{i,j}^{\rm obs}(V_k)$, and $\delta_{I_{i,j}^{\rm obs}(V_k)}$ are, respectively, the model intensity, the observed intensity, and the observed rms at the spatial pixel i, j and the velocity V_k.

The initial parameter set is crucial to obtain a converged solution. We adopted an iterative method to ensure convergence, repeating the 3D fitting where the best-fit parameters in the previous cycle were injected as the initial parameter set. The initial guess for the first cycle was obtained from a preparatory 2D fitting for the line moment-0 map and velocity field. The best-fit parameters and their uncertainties converged within eight cycles.

Uncertainties of the fitting parameters were obtained by a Monte Carlo method. We repeated 3D fittings for mock observed data cubes with randomly produced image-plane noise maps. The noise was spatially correlated on the appropriate beam scale, and its rms was scaled to the observed one. We adopted the best-fit values obtained from the real observed data cube as the most likely solution and the values in the central 68th percentile in the distribution obtained by the Monte Carlo method as their uncertainties.

In addition, we separately performed an exponential model fitting to the UV continuum image of the Hubble Space Telescope (HST) Wide Field Camera 3 (WFC3)/F160W filter. The fitting parameters are the central brightness, $A_{\rm UV}$, scale length, $r_{\rm UV}$, inclination, $i_{\rm UV}$, and position angle, $PA_{\rm UV}$. We also allowed a spatial offset of the UV central position $(x_{\rm UV,0}, y_{\rm UV,0})$ from the reference point in the source plane. A Gaussian point-spread function (PSF) with an FWHM of 0″15 of the HST/WFC3 IR channel (Skelton et al. 2014) was adopted for the

convolution in the fitting procedure in the image plane. In this particular case, we did not perform a Monte Carlo estimation of the uncertainties.

4.2. Result

Figure 3 shows a comparison between the observed and best-fit [O III] line cubes in the image plane. Figure 4 shows the source-plane reconstruction of the 2D [O III] line moment-0 map and velocity field from the best-fit line cube as well as the UV intensity map. Low residuals shown in these figures demonstrate a reasonably good fit. Table 1 presents a summary of the observed and derived properties of MACS1149-JD1. The inclinations, PAs, and central positions of the [O III] disk and the UV disk coincide with each other, while the scale lengths are different.

We have found $V_{\rm rot}/\sigma_V = 0.67^{+0.73}_{-0.26}$, whose range still permits a value greater than 1 consistent with a rotation-dominated system. This ratio is compared with similarly estimated values at lower redshift from the literature in the bottom panel of Figure 2. $V_{\rm rot}/\sigma_V$ of star-forming galaxies at $z < 4$ and $z \sim 6$ quasar host galaxies are well explained by a semiempirical model with a range of Toomre's disk instability parameter of $0.67 < Q_{\rm crit} < 2$ (Wisnioski et al. 2015). An extrapolation of the model indicates that MACS1149-JD1 at $z = 9.1$ has a quasistable disk composed of stars and gas: $Q_{\rm crit} \sim 2$ (Wisnioski et al. 2015).

5. Discussion

MACS1149-JD1 satisfies an empirical criterion for a rotation-dominated system, $\Delta V_{\rm obs}/2\sigma_{\rm tot} > 0.4$ (Förster Schreiber et al. 2009). Among the five criteria for a rotation disk (Wisnioski et al. 2015), the galaxy also satisfies (i) a continuous velocity gradient along a single axis, (ii) $V_{\rm rot}/\sigma_V > 1$ (but marginally), (iv) an agreement between photometric (UV) and kinematic ([O III]) axes ($<30°$), and (v) a positional agreement of the dynamical center ([O III]) and continuum centroid (UV). However, it does not satisfy criterion (iii) a positional agreement between the dynamical center and the velocity dispersion peak.

For the important criterion (ii), our dynamical model gives $V_{\rm rot}/\sigma_V = 0.67$ (0.41–1.40, 68% range), still indicative of a rotation, taking into account the possible range. We also examined a case where the [O III] emission and the dynamical disk are two different components in light of the two-component stellar populations discussed in H18. Namely, we considered five additional parameters of the central positions (x, y), inclination, PA, and scale length for the [O III] emission disk "decoupled" from the dynamical disk introduced in Section 4.1. As a result, we obtained a higher kinematic ratio of $V_{\rm rot}/\sigma_V = 1.4$. The dynamical disk center was spatially offset from the centers of [O III] emission and UV continuum arisen by the star-forming population, as found in cosmological simulations (e.g., Moriwaki et al. 2018). Although the fitting uncertainty was large due to the larger number of free parameters, this decoupled disk scenario would be very interesting to examine with the James Webb Space Telescope (JWST).

The criterion (iii) should also be discussed. The velocity dispersion peak is located ~ 1 kpc away from the [O III] disk center, possibly indicating a merger or an outflow. A possible small kink in UV emission around the dispersion peak
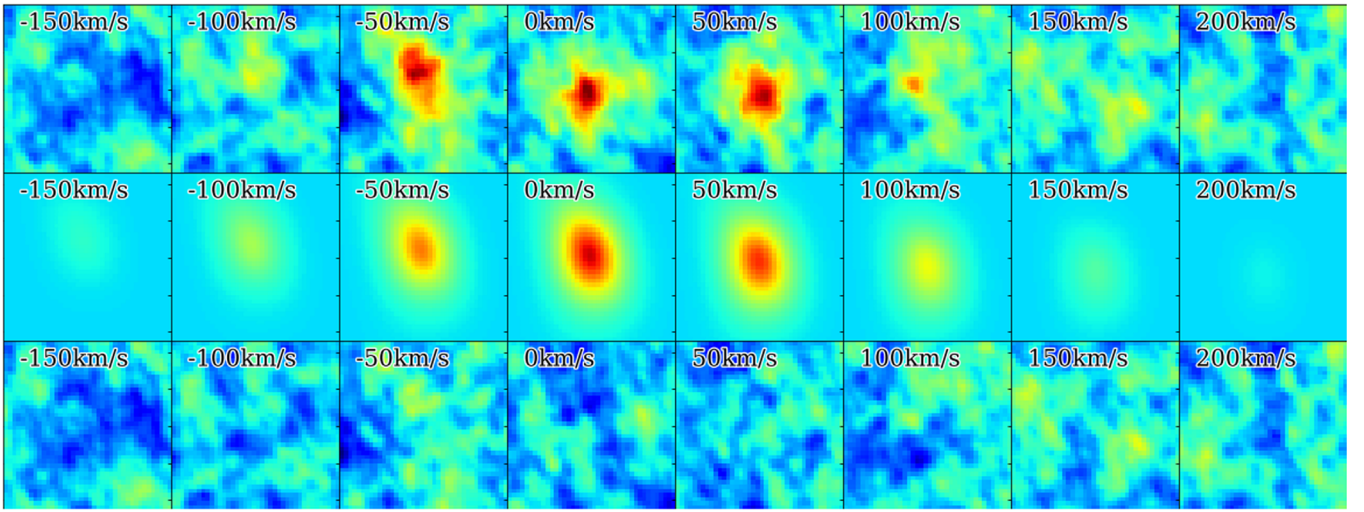
Figure 3. Image-plane channel map from -150 km s^{-1} (left) to $+200$ km s^{-1} (right) with a 50 km s^{-1} step. Top: the observed cube; middle: the model cube; bottom: the residual.
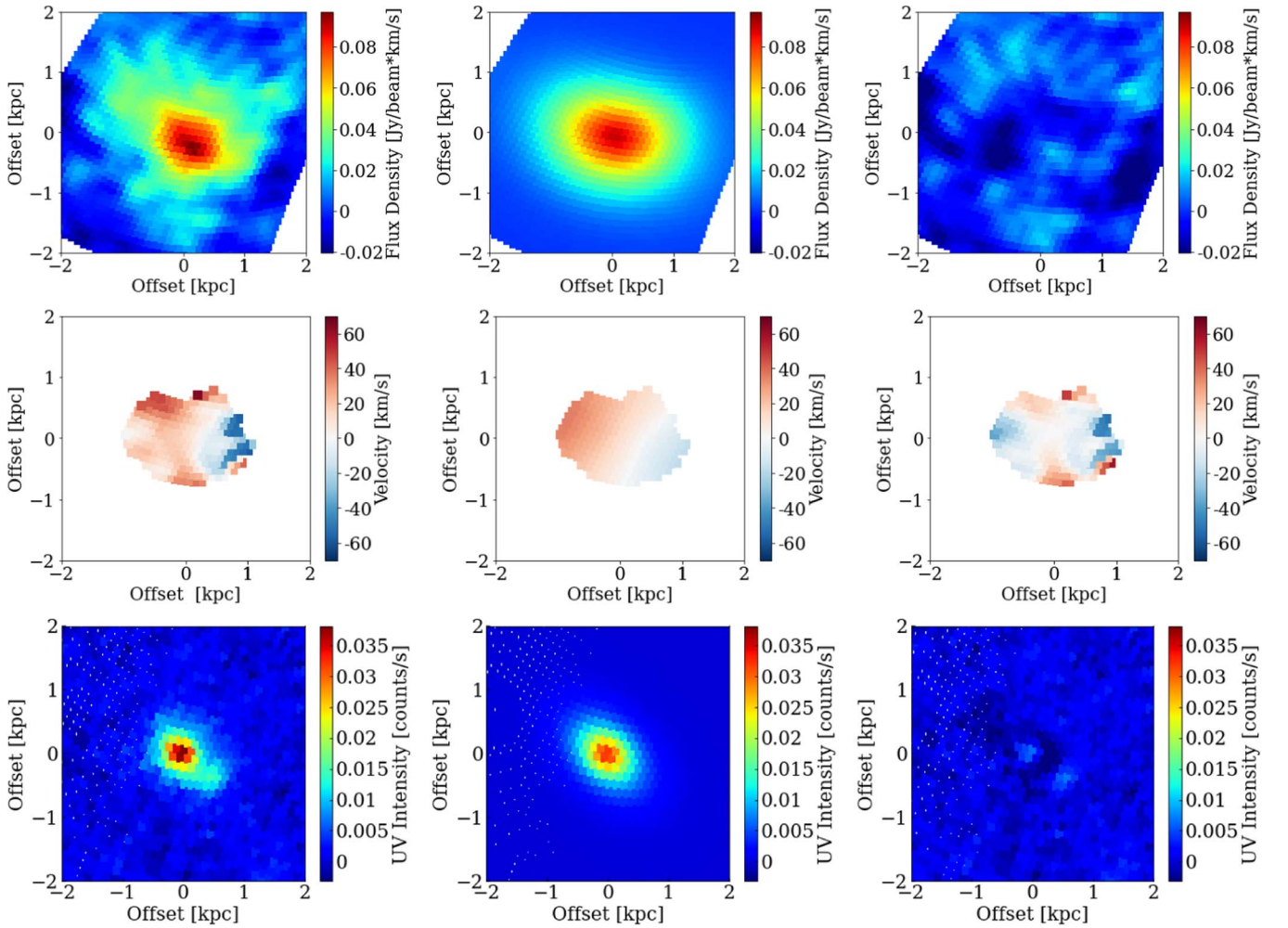
Figure 4. Top row: the [O III] 88 μm line moment-0 map; middle row: the [O III] line velocity field; bottom row: the UV continuum image. Left: the observations; middle: the models; right: the residuals. All images are shown in the source plane corrected for the gravitational lensing effect.

(Figure 1) might be a sign of a merger. The weaker Lyα line showing blueshift from the [O III] line (H18) may be another sign of a different component in the galaxy. However, there is no distinct structure in [O III] emission. We could not examine this possibility further with the current data set. The higher spatial resolution and sensitivity offered by JWST is required to address the merger possibility. In the following, we consider that MACS1149-JD1 is a rotating disk galaxy.

Table 1
A Summary of Properties of MACS1149-JD1

Property (1)	Value (2)	Remark (3)
Observed Values		
R.A. (ICRS)	$11^{\rm h}49^{\rm m}33^{\rm s}\!.58$	1
decl. (ICRS)	$+22°24'45''\!.7$	1
$z_{\rm spec}$	9.1096 ± 0.0006	1
M_* [$10^9\,M_\odot$]	$1.08^{+0.53}_{-0.18} \times (10/\mu)$	1
SFR [$M_\odot$ yr^{-1}]	$4.2^{+0.8}_{-1.1} \times (10/\mu)$	1
$\Delta V_{\rm obs}/2\sigma_{\rm tot}$	0.84 ± 0.23	2
Assumed Value: Lensing Magnification		
μ	4.7	3
Best-fit Values and Their 68th Percentile of the Dynamical Model		
$\Delta V_{\rm sys}$ [km s^{-1}]	10.3 (−0.5–20.2)	
$V_{\rm rot}$ [km s^{-1}]	46.7 (28.3–87.1)	4
σ_V [km s^{-1}]	69.9 (55.6–75.9)	
$V_{\rm rot}/\sigma_V$	0.67 (0.41–1.40)	5
$M_{\rm disk}$ [$10^9 M_\odot$]	0.65 (0.25–2.02)	6
$r_{\rm disk}$ [kpc]	0.50 (0.40–0.61)	6
$i_{\rm disk}$ [°]	56.8 (44.9–66.3)	
PA(disk) [°]	157.5 (143.2–168.4)	
Reduced χ^2 (Data cube)	1.18	
Best-fit Values of the UV Emission Model		
$r_{\rm UV}$ [kpc]	0.31	6
$i_{\rm UV}$ [°]	52	
PA(UV) [°]	138	
Δ(UV–disk) [kpc]	0.13 ± 0.2	6, 7
Reduced χ^2 (UV)	1.08	

Note. (1) Hashimoto et al. (2018). (2) This work. (3) `glafic` model: Kawamata et al. (2015) and Oguri (2010). (4) Derived from $M_{\rm disk}$ and $r_{\rm disk}$, not a fitting parameter. (5) Derived from $V_{\rm rot}$ and σ_V, not a fitting parameter. (6) Values in the source plane. (7) Systematic uncertainty in astrometry between the HST UV image and ALMA data cube is $0''\!.1$ (H18), corresponding to $\sim$0.2 kpc in the source plane.

The stellar mass of MACS1149-JD1 corrected by the `glafic` model ($\mu = 4.7$) is $2.3^{+1.1}_{-0.4} \times 10^9\,M_\odot$. The bulk of the mass is associated with the $\sim$300 Myr old mature stellar population, whereas $\sim$3 Myr old star-forming population is a minor component (H18). Crucially, the dynamical disk mass of $0.65^{+1.37}_{-0.40} \times 10^9\,M_\odot$ is consistent with that independently determined for the mature stellar population. If we consider the effect of the velocity dispersion in the case of $V_{\rm rot}/\sigma_V \sim 1$ (e.g., Burkert et al. 2010), the dynamical mass can be $\sim$5 times larger,[21] yielding $\sim$3 × $10^9\,M_\odot$, which is also consistent with the stellar mass of $\sim$2 × $10^9\,M_\odot$ (H18). Therefore, we conclude that the dynamical mass is attributable to the mature stellar population that formed at $z \sim 15$.

A cold gas component should exist in the galaxy because of the ongoing star formation. The gas mass fraction can be expressed as $f_{\rm gas} = (a/Q_{\rm crit})(\sigma_V/V_{\rm rot})$ with $a = 1$–2, depending on the velocity radial profile (Genzel et al. 2011; Wisnioski et al. 2015). Because $Q_{\rm crit} = 1$–2 for a stellar-plus-gas disk (e.g., Kim & Ostriker 2007; Genzel et al. 2011), the obtained $V_{\rm rot}/\sigma_V$ suggests $f_{\rm gas} \gtrsim 0.3$. Considering uncertainties in the estimated masses, it is possible that the $\sim$1 × $10^9\,M_\odot$ cold gas

---

[21] From Equation (11) in Burkert et al. (2016), one can derive the dynamical mass corrected for the turbulent pressure as $M_{\rm dyn} = M_{\rm disk} \times \{1 + 4.4(\sigma_V/V_{\rm rot})^2\}$ for $M_{\rm disk}$ and $V_{\rm rot}$ evaluated at $r = 2.2 r_{\rm disk}$ where the Freeman disk has the maximum rotation velocity (Freeman 1970).

component and $\sim$2 × $10^9\,M_\odot$ mature stellar population coexist, yielding $f_{\rm gas} \sim 0.3$ in a total mass of $\sim$3 × $10^9\,M_\odot$. The star formation rate of the galaxy is $8.9^{+1.7}_{-2.3}\,M_\odot$ yr^{-1} for the magnification $\mu = 4.7$ (H18). Hence, we obtain a gas depletion time of $t_{\rm dep} \sim 100$ Myr when the gas mass of $1 \times 10^9\,M_\odot$ agrees with an extrapolation of a mean relation of $t_{\rm dep} \sim 1.5/(1 + z)$ Gyr (Wisnioski et al. 2015) to $z = 9$.

The scale length in the source plane of [O III] disk is 1.6 times larger than that of the UV continuum. Notably, both scale lengths should be readily resolved by the ALMA beam and HST PSF sizes in the source plane ($\sim$0.3 and $\sim$0.1 kpc in radius, respectively). The [O III] emitting ionized gas should be powered by the young stellar population traced by UV. The extended distribution of the ionized gas compared to the young star cluster possibly suggests a significant escape of ionizing photons to a larger scale, and the galaxy may contribute to cosmic reionization. This may also explain the blueshift of the Lyα line (H18).

We have considered only a single mass component in the dynamical disk modeling. Because we are considering the very central part ($r \lesssim 1$ kpc) of the galaxy, the dark matter contribution is generally negligible (e.g., van Albada et al. 1985). According to Behroozi et al. (2019), the dark matter halo mass for a stellar mass of $\sim$10$^9\,M_\odot$ galaxy at $z = 9$ is $\sim$10$^{11}\,M_\odot$. The virial radius of such a halo would be $\sim$7 kpc in the proper coordinates (Dayal & Ferrara 2018). Therefore, our observations do not reach the halo scale yet; hence, neglecting its contribution is reasonable.

In conclusion, MACS1149-JD1 at $z = 9.1$ is the most distant galaxy with a signature of rotation. This is not contradictory to the concordance cosmological structure formation. Some theoretical studies predicted such a rotational disk in the earliest universe (e.g., Robertson et al. 2006; Katz et al. 2019). It is interesting to understand the role of two stellar populations proposed by H18 in the rotation disk formation. We suggest that the mass of the rotational disk is dominated by the mature stellar population formed in the first major star formation episode in this galaxy at $z \sim 15$ (H18). JWST's Guaranteed Time Observation programs targeting this galaxy will resolve the different spatial distributions of the young and mature stellar populations and confirm (or revise) the scenario.

ORCID iDs

Akio K. Inoue ⓘ https://orcid.org/0000-0002-7779-8677
Takuya Hashimoto ⓘ https://orcid.org/0000-0002-0898-4038
Richard S. Ellis ⓘ https://orcid.org/0000-0001-7782-7071
Nicolas Laporte ⓘ https://orcid.org/0000-0001-7459-6335
Yuma Sugahara ⓘ https://orcid.org/0000-0001-6958-7856
Hiroshi Matsuo ⓘ https://orcid.org/0000-0003-3278-2484
Yoichi Tamura ⓘ https://orcid.org/0000-0003-4807-8117
Yoshinobu Fudamoto ⓘ https://orcid.org/0000-0001-7440-8832
Kana Moriwaki ⓘ https://orcid.org/0000-0003-3349-4070
Guido Roberts-Borsani ⓘ https://orcid.org/0000-0002-4140-1367
Satoshi Yamanaka ⓘ https://orcid.org/0000-0002-7738-5290
Naoki Yoshida ⓘ https://orcid.org/0000-0001-7925-238X
Erik Zackrisson ⓘ https://orcid.org/0000-0003-1096-2636
Wei Zheng ⓘ https://orcid.org/0000-0002-0205-5174

References

Behroozi, P., Wechsler, R. H., Hearin, A. P., & Conroy, C. 2019, MNRAS, 488, 3143
Binggeli, C., Zackrisson, E., Ma, X., et al. 2019, MNRAS, 489, 3827
Bouwens, R. J., Bradley, L., Zitrin, A., et al. 2014, ApJ, 795, 126
Burkert, A., Förster Schreiber, N. M., Genzel, R., et al. 2016, ApJ, 826, 214
Burkert, A., Genzel, R., Bouch, N., et al. 2010, ApJ, 725, 2324
Dayal, P., & Ferrara, A. 2018, PhR, 780, 1
Di Teodoro, E. M., & Fraternali, F. 2015, MNRAS, 451, 3021
Förster Schreiber, N. M., Genzel, R., Bouché, N., et al. 2009, ApJ, 706, 1364
Freeman, K. C. 1970, ApJ, 160, 811
Genzel, R., Newman, S., Jones, T., et al. 2011, ApJ, 733, 101

Hashimoto, T., Inoue, A. K., Mawatari, K., et al. 2019, PASJ, 71, 71
Hashimoto, T., Laporte, N., Mawatari, K., et al. 2018, Natur, 557, 392
Hoag, A., Brada č, M., Brammer, G., et al. 2018, ApJ, 854, 39
Huang, K. H., Brada č, M., Lemaux, B. C., et al. 2016, ApJ, 817, 11
Inoue, A. K., Tamura, Y., Matsuo, H., et al. 2016, Sci, 352, 1559
Jones, T. A., Swinbank, A. M., Ellis, R. S., Richard, J., & Stark, D. P. 2010, MNRAS, 404, 1247
Katz, H., Galligan, T. P., Kimm, T., et al. 2019, MNRAS, 487, 5902
Kawamata, R., Ishigaki, M., Shimasaku, K., Oguri, M., & Ouchi, M. 2015, ApJ, 804, 103
Kim, W.-T., & Ostriker, E. C. 2007, ApJ, 660, 1232
Komatsu, E., Smith, K. M., Dunkley, J., et al. 2011, ApJS, 192, 18
Laporte, N., Meyer, R. A., Ellis, R. S., et al. 2021, MNRAS, 505, 3336
Lelli, F., Di Teodoro, E. M., Fraternali, F., et al. 2021, Sci, 371, 713
Lotz, J. M., Koekemoer, A., Coe, D., et al. 2017, ApJ, 837, 97
McMullin, J. P., Waters, B., Schiebel, D., Young, W., & Golap, K. 2007, in ASP Conf. Ser. 376, Astronomical Data Analysis Software and Systems XVI (San Francisco, CA: ASP), 127
Moriwaki, K., Yoshida, N., Shimizu, I., et al. 2018, MNRAS, 481, L84
Neeleman, M., Novak, M., Venemans, B. P., et al. 2021, ApJ, 911, 141
Oguri, M. 2010, PASJ, 62, 1017
Rizzo, F., Vegetti, S., Fraternali, F., Stacey, H. R., & Powell, D. 2021, MNRAS, 507, 3952
Rizzo, F., Vegetti, S., Powell, D., et al. 2020, Natur, 584, 201
Roberts-Borsani, G. W., Ellis, R. S., & Laporte, N. 2020, MNRAS, 497, 3440
Robertson, B., Bullock, J. S., Cox, T. J., et al. 2006, ApJ, 645, 986
Skelton, R. E., Whitaker, K. E., Momcheva, I. G., et al. 2014, ApJS, 214, 24
Smit, R., Bouwens, R. J., Carniani, S., et al. 2018, Natur, 553, 178
van Albada, T. S., Bahcall, J. N., Begeman, K., & Sancisi, R. 1985, ApJ, 295, 305
Watson, D., Christensen, L., Knudsen, K. K., et al. 2015, Natur, 519, 327
Wisnioski, E., Förster Schreiber, N. M., Wuyts, S., et al. 2015, ApJ, 799, 209
Zheng, W., Postman, M., Zitrin, A., et al. 2012, Natur, 489, 406
Zheng, W., Zitrin, A., Infante, L., et al. 2017, ApJ, 836, 210